13

The New Photo-Detectors for High Energy Physics and Nuclear Medicine

Nicola D'Ascenzo and Valeri Saveliev
National Research Nuclear University
Russia

1. Introduction

One of the main methods for the detection of the energy of the elementary particles is the conversion of the particle energy into light photons due to the scintillation process and then the conversion of the light photons into the electronic signal due to the photoelectric process (Scintillator/Photo-detector Detection Systems). These detection systems are widely used in high energy physics and currently operated in running experiments, as for example in the *CDF* experiment at Tevatron (CDFII, 1996) and in the *ATLAS* experiment at Large Hadron Collider (ATLAS, 1999). The same method is implemented in Nuclear Medicine and is widely used in clinical practice. Detection systems for Positron Emission Tomography (PET), Single-PET and Gamma Camera are based on scintillators read out by photo-detectors.
The main requirement of such applications is the necessity of the detection of a low photon flux. A typical number of scintillation photons produced by modern scintillating crystals is about 25 photons/keV and about 1 photon/keV is generated by a plastic organic scintillator.
For a long time the main photo-detector for such detection systems was the Photomultiplier Tube (PMT), which was created more than 50 years ago and has many well known disadvantages (Toshikaza et al., 2006).
As alternatives to the PMTs, in the last decade, a new type of photo-detector was developed on the basis of the semiconductor technology, the Silicon Photomultiplier (SiPM) (Golovin & Saveliev, 2004; 2000). At the present time such devices are produced by few companies as Multi Pixel Photon Counters (MPPC), Hamamatsu, Japan (Yamamura, 2009), SensL, Ireland (SensL, 2010)
The SiPM consists of an array of space-distributed micro sensors. Each micro sensor is capable of detecting a single quantum of light - the array is detecting the photon flux. This innovative detecting structure is a great technological improvement in the efficient detection of low photon fluxes. The SiPM is rapidly being used and proposed in many experimental physics and nuclear medicine applications. Few examples give the impression of the extension of use of such detectors: read-out of the fiber/scintillator detectors in the neutrino T2K experiment (Yokoyama, 2009), calorimeter systems at the International Linear Collider (ILD, 2009), CMS hadron calorimeter at the Large Hadron Collider (Freeman, 2009) and others. Many projects are active on the design of PET and Gamma camera using SiPM-crystal detectors (Herbert, 2006).
The aim of this chapter is to show the advantages of using the SiPM for the low photon fluxes detection in scintillator-based high energy physics and medical applications. The examples

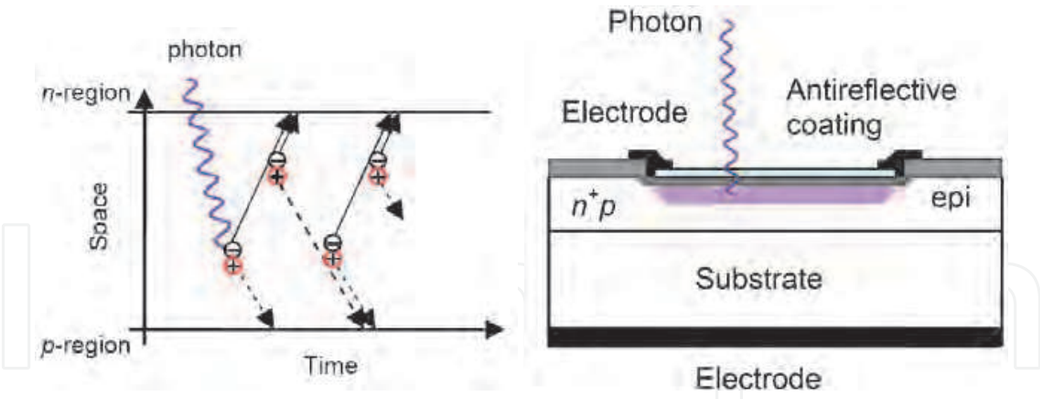

(a) (b)

Fig. 1. Schematic of the avalanche process (a) and schematic of the avalanche breakdown micro-cell of a Silicon Photomultiplier n on p type with virtual guard ring (Saveliev, 2010).

of the hadron calorimetry at the International Linear Collider and the new generation PET are considered and the potential of the interplay between mathematical modelling and experimental study is analysed in the design and optimization of such applications.

2. The Silicon Photomultiplier

2.1 Photo-detector structure

The SiPM is a semiconductor-based photo-detector developed for the detection of low photon fluxes. It consists of an array of micro-sensors (microcells), which are designed to detect a single quantum of light with high efficiency. They are based on a special geometry *pn* juntion (Golovin & Saveliev, 2004). Under a reverse bias a depleted area with a high in-built electric field is formed inside the structure. The interaction of a visible photon in the depleted area is mediated through the photo-electric effect with the consequent creation of one electron-hole (e/h) pair. The detection of such small signal is a general problem due to the thermal noise of the detector itself and of the front-end electronics (Alvares-Gaume, 2008). The SiPM has the possibility of the detection of a single photon or single e/h pair through a very high intrinsic gain of the order of 10^6. The amplification is achieved by the avalanche breakdown process due to secondary impact ionization (Tsang, 1985). The schematics of the amplification process in one microcell of the SiPM is shown in Fig. 1a. When the e/h pair is created by a photon interaction, as in the figure, both the generated electron and hole are accelerated in the electric field and reach an energy higher than the ionization energy of the valence electrons and holes in the semiconductor. This initiates a self-sustaining avalanche process. The current rises exponentially with time and reaches the breakdown condition. The avalanche process is stopped via a quenching mechanism obtained by a serial resistor to every microcell. The rising current flows out from the microcell through a quenching resistor causing a voltage drop on the resistor and accordingly to the *pn* junction bias voltage. When the build-in electric field is lowered enough, the avalanche stops. After the quenching, a hold-off time is required to the microcell in order to restore the proper build-in electric field. The resulting intrinsic gain of the microcell is about 10^6 electrons per detected photon, which is well above the noise level of modern measurement electronics. A structure of the Silicon Avalanche Breakdown micro-cell is shown in Fig. 1b. The structure consists of a silicon substrate with a *p*-type epitaxial layer (epi). The avalanche breakdown structure

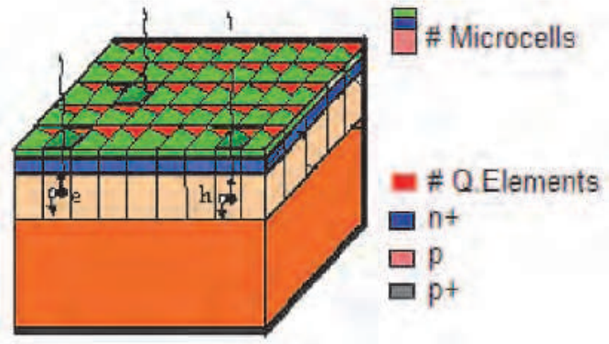

Fig. 2. Equivalent schematic of the structure of the Silicon Photomultiplier (Saveliev, 2010).

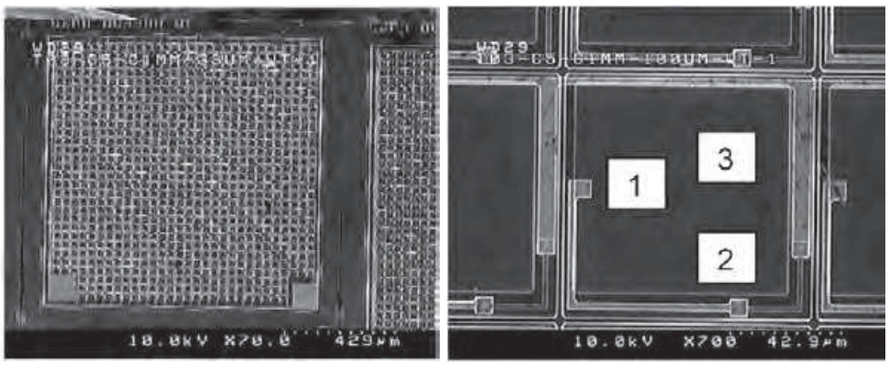

(a) (b)

Fig. 3. Micro image of a modern Silicon Photomultiplier. Overall view 1×1 mm^2 (a) and detailed view of the microcell area (b) (Saveliev, 2010).

is represented by the shallow *pn* junction (n^+p) in the silicon epitaxial layer with the so called virtual guard ring designed to prevent peripheral avalanche breakdown processes. The heavily doped n^+ region is connected to one electrode through a serial quenching resistor. The second electrode is formed on the back side of the substrate. The *pn* junction is designed to reach a very high in-build electric field of the order of 10^5 V/cm within the small thickness of the silicon layer of the order of few microns.

The schematic structure of the modern SiPM is shown in Fig. 2. It consists of an array of the above described *pn* junctions micro-cells (light grey squares) of typical size 30×30 μm^2 on a total sensitive area of few mm^2. Each microcell has the quenching element located close to the *pn* junction (grey and marked as Q element). The microcells are connected in parallel through a common electrode. The sum of signals from the array provides an output signal proportional to the number of detected photons.

The topology of the SiPM is shown on Fig. 3. On Fig. 3a is shown the top view of 1 mm^2 SiPM with micro-cells size about 30×30 μm^2. The total number of micro-cells is 1000 on 1 mm^2. The typical size of Silicon Photomultipliers is 1×1 mm^2 (up to 5×5 mm^2 without significant degradations in performances). In Fig. 3b is presented the microscopic view of a single avalanche breakdown micro-cell where the main elements of the structure are visible: the sensitive area (1), the quenching element (2), a part of the common electrode system (3). The microcells are also optically isolated in order to reduce the probability that optical photons

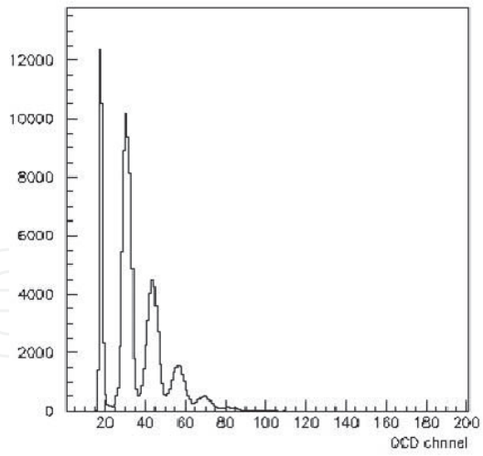

Fig. 4. Spectrum of a low photon flux signal in a SiPM.

produced in the avalanche process initiate an avalanche in neighbouring cells. The optical trenches around each microcell are also visible in the figure.

2.2 Silicon Photomultiplier performance

2.2.1 Single photon detection

The most challenging characteristic of the photo-detectors is the possibility of excellent single photon detection performance. The spectrum of a low photon flux detected with a SiPM is shown in Fig 4. The measurement is performed at room temperature. The resolution of the SiPM allows a precise analysis of the detected photon flux. The structure of the spectrum shows well defined peaks corresponding to the number of detected photons. The first peak corresponds to the noise of the measurement electronics (pedestal). The second peak corresponds to one photon detected, the third peak corresponds to two photons detected and so on. The typical Poisson distribution characterizing the photon statistic describes the spectrum. The SiPM introduces a significant improvement in the possibility of single photon detection in comparison with the traditional photomultiplier tubes (Toshikaza et al., 2006).

2.2.2 Photon detection efficiency of SiPM

The photon detection efficiency (PDE) of the Silicon Photomultiplier could be defined as:

$$PDE = \eta(\lambda) \cdot P_b(V) \cdot F \tag{1}$$

where $\eta(\lambda)$ is the quantum efficiency of the Silicon microcell structure, $P_b(V)$ is the probability of the avalanche breakdown in the silicon microcell structure, F is the filling factor of structure geometry (Saveliev, 2010).

The experimental determination of the photon detection efficiency of the SiPM is usually performed in two steps. First the photo detection probability of a single micro cell is measured relative to a calibrated photo detector with a monochromator light source. Then the result is rescaled to a full area SiPM multiplying by the filling factor, which in modern technologies is within the range 0.6–0.8.

The measured photon detection efficiency of the SiPM is shown in Fig. 5 as a function of the wavelength at 2V above the breakdown voltage. The PDE reaches a peak value of about 20% at around 500 nm. The quantum efficiency of photocathodes used in PMT shows a maximum

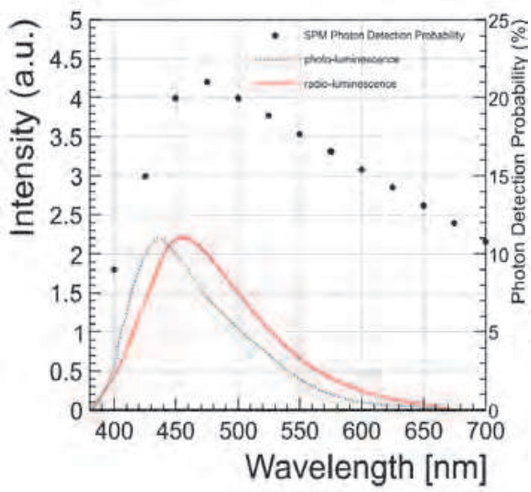

Fig. 5. Photon detection efficiency of the SiPM (black dots) Stewart (2008). Spectra of photo-luminescence (blue dotted line) and radio-luminescence (red continuous line) of a LSO crystal (Mao, 2008).

of 20-30 % within a spectral region between 350 nm and 500 nm (Toshikaza et al., 2006). Improvements are ongoing in the SiPM technology in order to achieve a high photon detection efficiency including the increasing the sensitivity in the blue spectral region. A realistic value of the photon detection efficiency of modern SiPM is $40 - 60\%$.
In the same Fig. 5 the photo-luminescence and radio-luminescence emission spectra of *LSO* are shown according to the reported experimental measurements (Mao, 2008). It is observed that the peak of the emission spectrum is 420 nm for the photo-luminescence and 450 nm for the radio-luminescence. The red shift of the radio-luminescence spectrum is probably due to a higher contribution of the irregular luminescence centre *Ce*2. The photon detection efficiency of the SiPM matches the requirements for the read-out of the scintillation light from *LSO*.

2.2.3 Time performance of SiPM

The time performance of the SiPM is defined by two factors: the rising time of the avalanche breakdown signal and the recovery time, which is defined by the process of reconstruction of the *pn* junction state after quenching the avalanche breakdown process and recharging through the quenching resistor. The rising time is defined by the generation time of the avalanche breakdown process and is characterized by the drift time of carriers under the high electric field. The drift velocity of the carriers under electric field of about 10^5V/cm is limited by the scattering process and in silicon structures it is approximately 10^7 cm$\times$ s^{-1}. As an example for the thickness of a depleted area of 4 microns the rising time is about 30 ps (Saveliev, 2010). The time resolution of the SiPM is measured as 27.54 ps, including the response of measurement system (Stewart, 2008).

2.2.4 Dynamic range and linearity of SiPM

The detection of photons by a silicon Photomultiplier is a statistical process based on the probability of detecting randomly space-distributed photons by the limited number of space-distributed sensitive elements. The photon detection efficiency and the total number of micro-cells determine the dynamic range of the Silicon Photomultiplier. The number

of detected photons n_{dph} (number of micro-cells with signal) as function of the number of incident photons can be approximated by the following expression:

$$n_{dph} = N_{mic}\left(1 - e^{-\frac{PDE \cdot N_{ph}}{N_{mc}}}\right) \quad (2)$$

where N_{mc} is the total number of microcells, N_{ph} is the number of incident photons and PDE is the photon detection efficiency.
The Silicon Photomultiplier response is linear when the number of incident photons is much less than the total number of micro-cells. The Silicon Photomultiplier response begins to saturate when the number of fired pixels reaches approximately a quarter of the total number of micro-cells, but could be corrected by well known statistical functions (Saveliev, 2010).

2.2.5 Dark rate of SiPM

One of the main factors limiting the performance of the Silicon Photomultiplier is the dark rate. The dark rate is the frequency of a thermal e/h pair created in the sensitive area of the SiPM. Such e/h pair generates an output signal with amplitude equivalent of a single photon signal and could not distinguished from it. The typical dark rate value for the modern Silicon Photomultipliers is in the range 0.1-1 MHz per mm^2 (Saveliev, 2010).
The amplitude of the dark rate pulses is equivalent to the single photon signal amplitude and in applications dealing with tens-hundred of photons it could be neglected. For applications with very low photon flux the average dark rate can be measured and subtracted. However, the statistical variation in the dark rate cannot be subtracted and constitutes a noise source that determines the minimum detectable signal. As the dark rate of the Silicon Photomultiplier scales as its area and the acceptable dark rate is about 10^6 in low photon flux, the maximum designable area is limited to around few mm^2.

3. Recent advances of scintillator/SiPM detection systems in high energy physics

3.1 The scintillator/SiPM detection system for highly granular hadron calorimetry

A modern concept of high energy physics detection systems is the particle flow algorithm (PFA) (Thompson, 2007). This method is proposed for the experiment at International Linear Collider (ILD, 2009). Instead of performing a pure calorimetric measurement, as in traditional environments, the reconstruction of the four vectors of all the observable particles in the jet is proposed. The reconstructed jet energy is the sum of the energy of the individual particles. The momentum of the charged particles is measured in the tracker, while the energy of the neutral particles is measured in the calorimeters. The electromagnetic calorimeter is used for the measurement of the energy of photons and for the identification of photons and electrons. The hadronic calorimeter is used for the measurement of the energy of neutral hadrons and for the identification of hadrons. The muon chambers are used for the identification of muons. A detector optimized for the particle flow should have an excellent separation power of the components of the jets. The most important features in this respect are the spatial separation of the particles in the high energy jets, which is achieved with a high magnetic field, and high space resolution systems including the calorimeter systems. The key point of the hadron calorimetry designed for the particle flow technique is the granularity. It allows in fact to identify the single particles through the morphological properties of the shower. The calorimeter becomes an imaging device more than an energy measurement device.
Mathematical modelling studies were performed for the optimization of the performances of

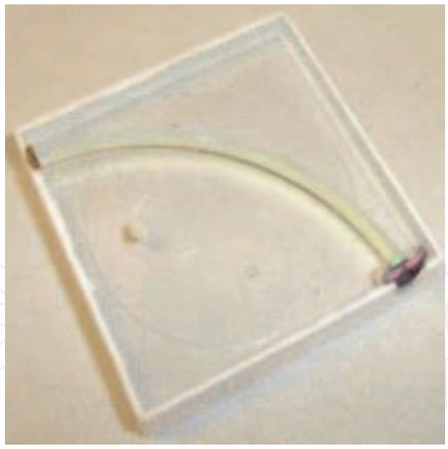

Fig. 6. Design of the scintillator/SiPM detection system for hadron calorimetry. The green sensitive SiPM is coupled to the scintillator through a wavelength shifter fiber (CALICE, 2010).

the hadron calorimeter for the International Linear Collider. It is shown that a transverse segmentation of 3×3 cm^2 and a longitudinal segmentation of about 1 cm satisfies the requirements in the experiment. Such modern performance calorimeter system, especially the hadron calorimeter, could be developed only on the basis of new technologies (ILD, 2009). One of the solutions is to use the modern scintillator/SiPM detection system.

The first proposed design of the scintillator/SiPM detection system consists of a $3 \times 3 \times 0.5$ cm^3 plastic organic scintillator tile read-out individually by a Silicon Photomultiplier (Fig. 6). The coupling between the scintillator and the photo-detector is performed via a wavelength shifter fiber. The scintillator/photo-detector system was optimized to yield about 15 photons on average in response to a minimum ionizing particle.

A simplification of the coupling between SiPM ad scintillator would be highly desirable, in order to extend the concept to a large scale detector. The new generation of SiPMs produced by Hamamatsu (MPPC) shows a better optical sensitivity in the 420 nm spectral region, making it possible to investigate the direct read-out of the scintillation tile (D'Ascenzo et al., 2007).

3.2 Mathematical model of a highly granular calorimeter based on scintillator/SiPM with individual read-out

In order to estimate and optimize the performance of the detection system with SiPM, a mathematical model of a scintillator/SiPM calorimeter is performed on the basis of the GEANT4 simulation framework. It allows to include the geometry and the physics processes in response to any final states resulting from the studied high energy particle collisions. The result of the simulation has maximal flexibility and can be studied with the same reconstruction and statistical analysis techniques developed for the application to real data.

The mathematical model includes a detailed geometrical description of the full detector system. The components of the mathematical model are shown in Fig. 7. In the barrel region the detector components are the vertex detectors (VTX, SIT), the tracker (TPC, SET), the electromagnetic and hadronic calorimeters (ECAL, HCAL) and the return yoke with muon system (YOKE). In the forward region the forward tracking detectors (FTD, ETD) the luminosity (LCAL, LHCAL) and veto detectors (BCAL) are included.

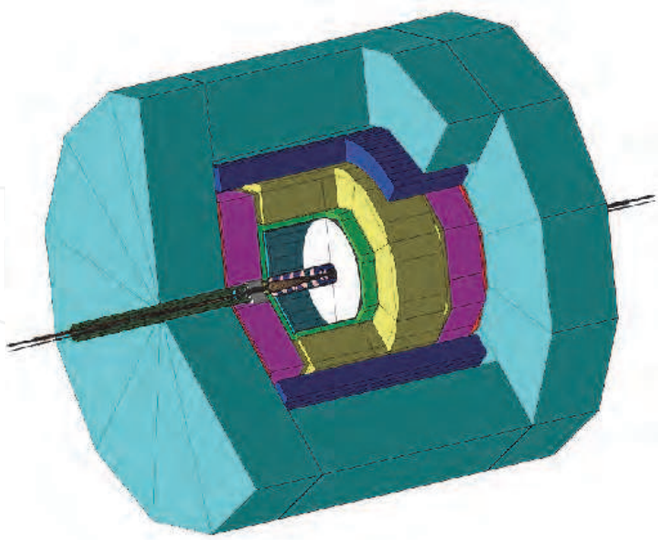

Fig. 7. Mathematical model of the detector for the International Linear Collider. The overview of the detector components is shown. From the inside to the outside, the detector components are the vertex detectors (VTX, SIT), the tracker (TPC, SET), the electromagnetic and hadronic calorimeters (ECAL, HCAL) and the return yoke with muon system (YOKE). In the forward region the forward tracking detectors (FTD, ETD) the luminosity (LCAL, LHCAL) and veto detectors (BCAL) are included (ILD, 2009).

The hadronic calorimeter consists of one barrel and two end-cap modules. The barrel module has octagonal shape with inner and outer radius respectively of 2.02 m and 3.33 m. The end cap modules has also octagonal shape and has a longitudinal thickness of 1.3 m, inner and outer radius of 329 cm and 3.33 m. Each module is composed of 40 layers in an alternating structure of 0.5 cm thick plastic scintillators as active material and 1 cm thick stainless steel as absorber.

The detailed geometry of the scintillator/SiPM detection system is introduced in the simulation. Each scintillator layer is segmented in 3×3 cm^2 scintillator tiles, individually read out by a SiPM. The total amount of calorimeter cells is about 10^6. The energy deposited in each cell is independently calculated and stored for further analysis.

The response of the scintillator/SiPM detection system is introduced with a parametric model based on the results of the experimental study of the hadron calorimeter system prototype (CALICE, 2010).

The detector is immersed in a magnetic field of 3.5 T.

The reconstruction of the particles in the final state from the simulated detector response is performed with a reconstruction software based on the Particle Flow Algorithm.

The dependence of the jet energy resolution on the size of the sensitive cells of the hadronic calorimeter is shown in Fig. 8. The energy resolution of jets with energy as low as 45 GeV is independent from the size of the HCAL cell, while higher energetic jets show a stronger dependence on the granularity of the hadronic calorimeter. This effect is due to the increased complication of the structures in the hadronic calorimeter in response to higher energy jets.

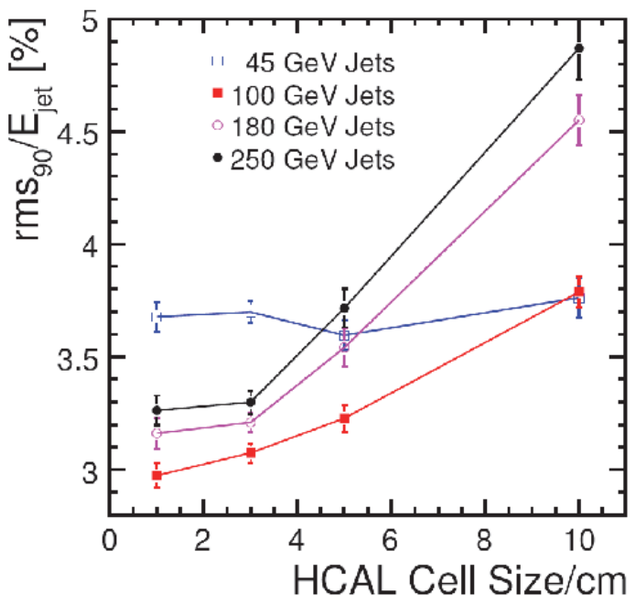

Fig. 8. Monte Carlo estimation of the dependence of the jet energy resolution on the sensitive element size of the highly granular hadronic calorimeter based on scintillator/SiPM detection system with individual read-out (ILD, 2009).

Consequently the best possible granularity is needed in order to identify each contribution. The result indicates that the ILC jet energy resolution goal is achieved with a 3×3 cm^2 scintillator tile segmentation (ILD, 2009).

3.3 Experimental study of the prototype of the highly granular hadron calorimeter based on scintillator/SiPM with individual read-out

The experimental study of the new detection system on the basis of scintillator/SiPM photo-detectors for application in highly granular hadron calorimeters was performed on a prototype of hadron calorimeter. The prototype consists of a sampling structure alternating 2 cm thick absorber steel plates with 0.5 cm thick sensitive layers. It has a total surface of 90×90 cm^2 and consists of 38 layers, for a total length of 5 λ_0.

Each sensitive layer is a array of 216 scintillators. The 30×30 cm^2 core has a granularity of 3×3 cm^2 and the outer region is equipped with tiles of increasing size — 6×6 cm^2 and 12×12 cm^2. Each scintillation tile is read-out individually by a SiPM (Fig. 6). The coupling between the scintillator and the photo-detector is performed via a wavelength shifter fibre arc (Kurakay WLS fiber Y11(200)). The fibre is inserted in a groove carved directly in the tile. A mirror is placed on one side of the tile in order to minimize the light losses along the fibre. The photo detector is installed directly on the tile coupled to a WLS fiber. A 3M reflector foil is applied on the surface of the tiles. The sensitive layer is housed in a steel cassette, with 2 cm thick rear and front plates. The calibration of the photo-detectors with light is done with a LED/clear fibre system. The fibres are embedded with the sensitive cassette itself and a proper electronic board controls the LED system (CALICE, 2010).

The electronic read-out of the signals of the Silicon Photomultipliers is made by the special electronics ILC-SiPM chip with 18 channels, each composed of a variable-gain,

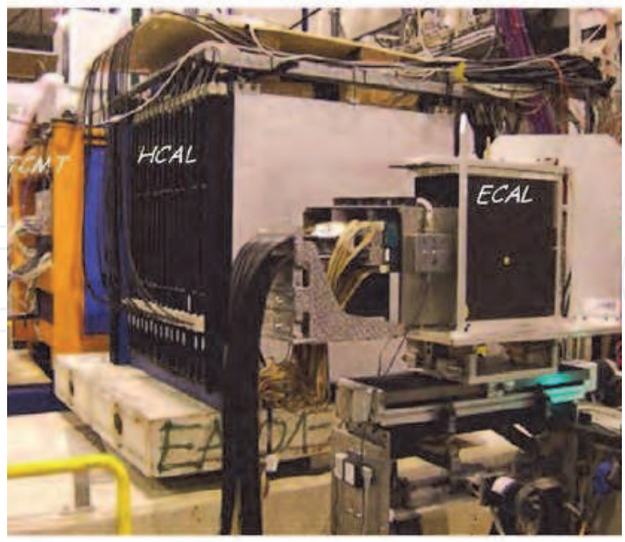

Fig. 9. Set-up of the detectors in the CERN test beam. The AHCAL was tested in combination with a prototype of highly granular Silicon/Tungsten electromagnetic calorimeter (ECAL) and a strip-scintillator/steel Muon Tracker Tail Catcher (TCMT) (Behnke, 2007).

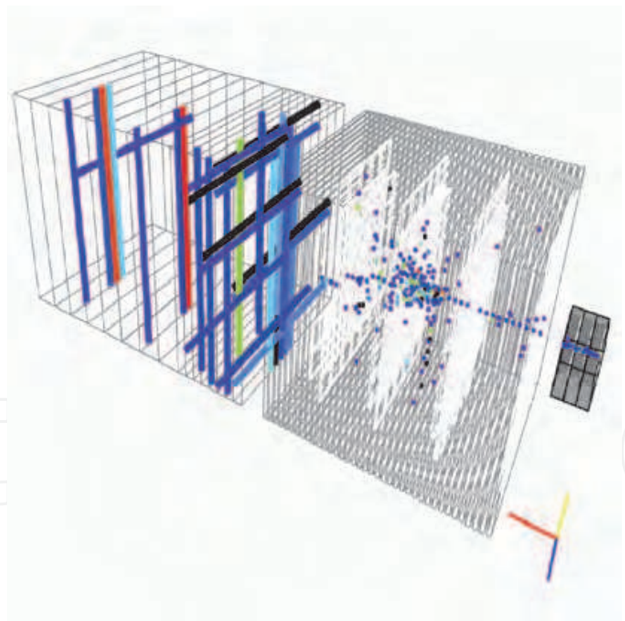

Fig. 10. Pion shower (12 GeV) identified in the data (CALICE, 2010).

charge-sensitive amplifier, a variable shaper, track and hold stage and a multiplexing unit (Blin, 2006).

The analog hadron calorimeter (AHCAL) was tested in combination with the prototypes of the highly granular silicon-tungsten electromagnetic calorimeter (ECAL) and of the scintillator strip tail catcher (TCMT) at the H6 beam line of the CERN SPS facility. The experimental

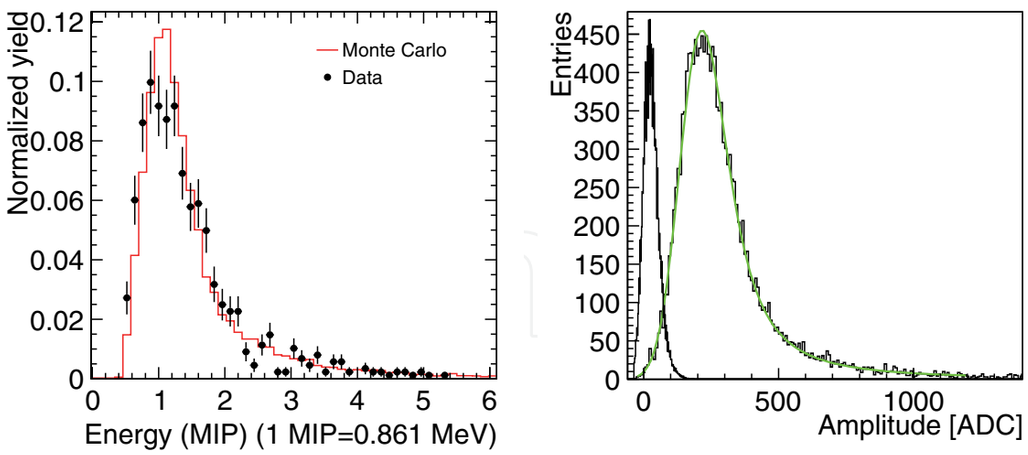

(a) (b)

Fig. 11. Response spectrum of a scintillator/SiPM detection system to muons in the hadronic calorimeter prototype (CALICE, 2010; D'Ascenzo, 2009).

setup is shown in Fig. 9.
The 450 GeV proton beam is used on a Beryllium target in order to generate a secondary beam of pions with a wide momentum spectrum in the range between 30 GeV/c and 205 GeV/c. In addition, a muon beam is also available due to contamination of the secondary pion beam. The average muon energy is hence approximately $0.8 \cdot E_{\pi}$.
A mathematical model of the test setup system based on the GEANT4 simulation framework is also implemented on the basis of the mathematical model of the full detection system. The simulation includes all the detailed components of the test beam experimental setup.
The first important goal of experimental study is the verification of the efficient detection of the high energetic particles, minimum ionizing particle (m.i.p.), as required by the PFA concept. As an example a 12 GeV pion shower identified in the data is shown in Fig. 10. Furthermore muons produced in the hadron shower are also identified as straight tracks which escape from the calorimeter and penetrate the tail catcher (D'Ascenzo, 2009). The study of the response to muons, which mainly deposit energy by the ionization process in the massive volume of matter, could give a good experimental evidence.
Fig. 11a shows the signal of a single calorimeter scintillator cell read-out by a SiPM produced by 120 GeV muons. On the same plot is presented the Monte Carlo result including the systematic effects of the detector. The experimental results are well described by the mathematical model.
The resolution of the m.i.p. signal in a scintillator cell of the hadronic calorimeter depends on the statistical effects of the photon detection. The poisson fluctuation of the number of photo-electrons ($N_{p.e.}$) generated in the SiPM is the main source of the smearing of the signal. Its effect on the resolution of the visible energy depends on the $\sqrt{N_{p.e.}}$; the most probable value of the m.i.p. signal is 861 keV and corresponds to 15 ± 3 photo-electrons, with a consequent relative statistical fluctuation of $\sqrt{15}/15 = 25\%$. Moreover, the poisson smearing doesn't affect the energy deposited in the single cell uniformly. According to a simulation of the energy response of the single AHCAL cell to muons, a Landau distribution with Most Probable Value at 861 keV and width 60 keV approximates the energy deposited in

the scintillator. The resolution is $60/861 \sim 5\%$.
The muon signal measured in the data can be fitted with a Landau distribution convoluted with a Gaussian distribution, which models the smearing of the detector read-out. The result of the fit of the response of a single cell to a 120 GeV muon is shown in Fig. 11b. The energy resolution of the m.i.p. signal is about 70% but the signal is well distinguished from the noise pedestal. In the full prototype an average S/N separation of about 9 is measured (CALICE, 2010).

4. Recent advances of scintillator/SiPM detection systems in nuclear medicine

4.1 The scintillator/SiPM detection system in Positron Emission Tomography

Positron Emission Tomography is a powerful functional imaging modality that provides dynamic, quantitative information on the biological characteristics of tumours and other tissues. While PET has mainly found clinical application in oncology, uses in cardiology, neurology and neuropsychiatry are expected to increase in the future. Recent studies showed the potential of PET for the measurement of tissue activation and perfusion in specific diseases, as brain neurological perfusion in Alzheimer and autism or hearth activation study in case of myocardial infarction (Boddaert & Zilbovicius, 2006; Buchsbaum, 2006).
It is required to develop various PET systems with significantly better performance than commercially available scanners, in particular concerning spatial resolution for earlier cancer detection and more accurate staging. Also the PET camera needs higher sensitivity to reduce scanning time, cost and patient exposure to radiation, good time resolution, operation at high magnetic fields for a combination with Magnetic Resonance Techniques and design flexibility. The detection system of PET is the key point which defines the main performance of the medical imaging systems and which is triggering the new clinical applications and new developments in molecular and cell biology. The modern advances in the SiPM development made it possible to develop a new type of scintillation crystals/SiPM detection system for application in Positron Emission Tomography.
The miniature size and the low material budget of SiPMs give the possibility to build flexible PET detection systems and include complementary methods for improving the performance. This feature is referred to as the depth of interaction (DOI) problem. The measurement of the DOI is realised quite simply with SiPMs and will improve imaging quality. The excellent time resolution of SiPMs and of the new scintillators gives the possibility of using the Time of Flight methods with a significant improvement of the signal to noise ratio of PET images. The effect on PET would be the ability to reduce the coincidence timing window by one order of magnitude. This would not only result in improvements in the noise equivalent counts (NEC) through the reduction in randoms, but also provides the ability to perform time-of-flight PET reconstruction. With a timing resolution of less than 0.5 ns, it becomes possible to define the site of positron annihilation within a line segment of less than 7.5 cm, and thereby to improve the reconstruction.

4.2 Mathematical model of a PET scanner based on LSO/SiPM detectors with individual read-out of crystals

In order to estimate the possibility to achieve the mentioned goals, a mathematical simulation study of a PET scanner with LSO crystals individually read-out by a SiPM is performed. The mathematical model for the LSO/SiPM detection system is developed on the basis of the GATE framework, which allows to include the geometry and the physics processes and also to perform the reconstruction by standard methods for the performance study (Strul, 2003).

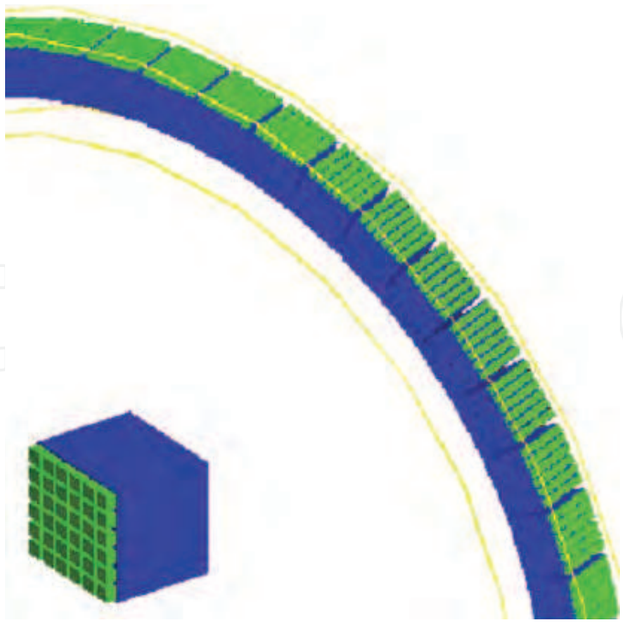

Fig. 12. Detailed geometry of the PET detection system on the basis of LSO scintillator crystal read-out individually by SiPM.

A detailed geometrical configuration of a detector ring for a PET scanner based on the LSO/SiPM detection system is shown in Fig. 12. One ring of 53.3 cm diameter is composed of detection modules placed around the axis in a cylindrical symmetry. The size of the system is typical of the state of the art high resolution brain PET scanners (Karp et al., 2003).
According to the NEMA NU2-2001 performance protocol (National Electrical Manufacturers Association, 2001) the source configuration used for the estimation of the space resolution is the β^+ emitter ^{18}F, arranged in a glass spherical capillary with internal and external radius respectively of 0.2 mm and 0.3 mm.. The initial activity is 10000 Bq.
Each detector module consists of a 6×6 array of LSO/SiPM cell. As an example, in case of $3 \times 3 \times 25$ mm^3 crystals, the crystals pitch is 3.1 mm and the size of one detector module is $18.6 \times 18.6 \times 2.5$ mm^3. The ring is composed of 85 modules with an angular pitch of 4.23°. LSO crystals are covered by a reflecting layer of Teflon, with the correct description of the physical and optical properties. The geometrical acceptance and the optic coupling of the crystals with the SiPM are included according to experimental estimations.
Light propagation and collection on the face of SiPMs are also included in the physics processes. The Photon Detection Efficiency of the SiPMs used in the simulation is shown in Fig. 5 and is reported from experimental measurements (Stewart, 2008).
The energy deposited in each crystal is calculated in the simulation and is converted into a photon flux via the scintillation processes. The scintillation photons are produced as gaussian distributed with a mean value (LY) of 27000 photons/MeV (Melcher, 1992) and a variance σ_{sc} equal to the expected Poisson statistic variance multiplied by a scale factor: $\sigma_{sc} = \alpha_s \sqrt{LY \times E_\gamma}$, where E_γ is the energy of the detected photon. The scale factor $\alpha_s = 4.41$ models the intrinsic not-linearity of LSO. The photon yield of each crystal is read-out independently by a SiPM and the detected light output of each SiPM is calculated.
The timing performance is included in the simulation as the scintillation process time dependence and the light propagation. The intrinsic time resolution of the SiPM is also

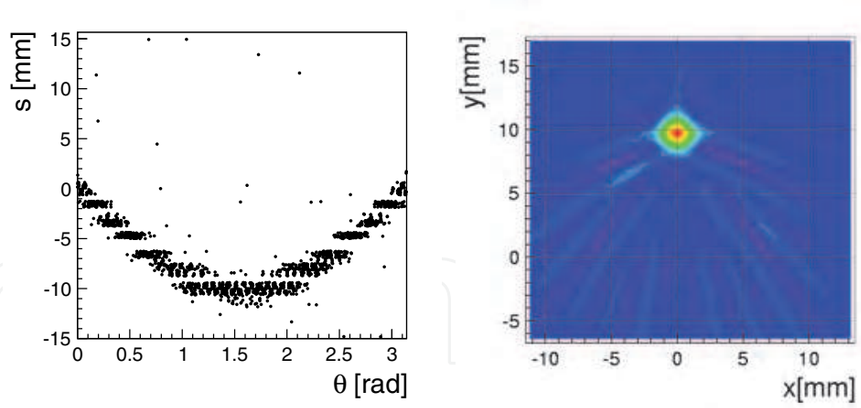

(a) (b)

Fig. 13. Sinogram (a) and reconstructed image (b) resulting from the simulation of the response of the PET system based on LSO/SPM detectors to a ^{18}F source of 0.2 mm radius placed at a vertical distance of 1 cm from the centre of the tomograph. The detection module is composed of a 6×6 array of $3 \times 3 \times 25$ mm^3 LSO crystals.

considered in the simulation.
The coincidence condition is defined as two events in two opposite crystals with deposited energy within $\pm 3\sigma$ around the photo-peak and within a coincidence time window of 80 ns.
The reconstruction of the Lines Of Response (LOR) is performed by using the position of the centre of the two crystals found in coincidence. The sinogram is constructed from the LORs, without applying any rebinning or geometrical correction. A standard filtered backprojection algorithm FBP2 with Hammer filtering is applied to the sinogram for the reconstruction of the original image and for the study of the spatial resolution. The sinogram resulting from the simulation of the response of the PET system is shown in Fig.13a. As any rebinning is applied, the structure of the LSO array composing the detector block is visible. The reconstructed image is shown in Fig.13b. The transverse spatial resolution is estimated as $\sigma_x = (0.94 \pm 0.62)$ mm and $\sigma_y = (0.87 \pm 0.46)$ mm. The estimated average transverse resolution (FWHM) is (2.13 ± 1.26) mm. The axial resolution depends uniquely on the ring thickness. In this example case of a detecting module consisting of a 6×6 array of $3 \times 3 \times 25$ mm^3 LSO crystals, the ring thickness is 18.6 mm. The corresponding axial resolution is estimated as about $18.6/3.0 = 6.2$ mm.
The results of the study are shown on Fig. 14. The space resolution is studied of PET systems based on 6×6 arrays of $3 \times 3 \times 25$ mm^3, $4 \times 4 \times 25$ mm^3 and $5 \times 5 \times 25$ mm^3 individually read-out LSO crystals. The transverse space resolution (FWHM) ranges between about 2 mm and 4 mm. For a comparison with results reported in literature, a transverse spatial resolution of 4 mm was measured for a high resolution brain PET scanner based on an Anger-logic detector array with 4×4 mm^2 GSO crystals (Karp et al., 2003). The single crystal read-out introduces hence a sensitive improvement with respect to the traditional Anger-logic based PET systems. The axial resolution ranges between about 6 mm and 10 mm. These value refer to the ring thickness calculated using a 6×6 array of LSO crystals. The flexibility of the LSO/SPM detection system allows to optimize the ring thickness according to the specific clinical needs of the tomograph, resulting in lower or higher axial resolution.
The mathematical simulation shows a significant improvement of the performances and flexibility of the PET detection systems based on scintillator/SiPM detection systems.

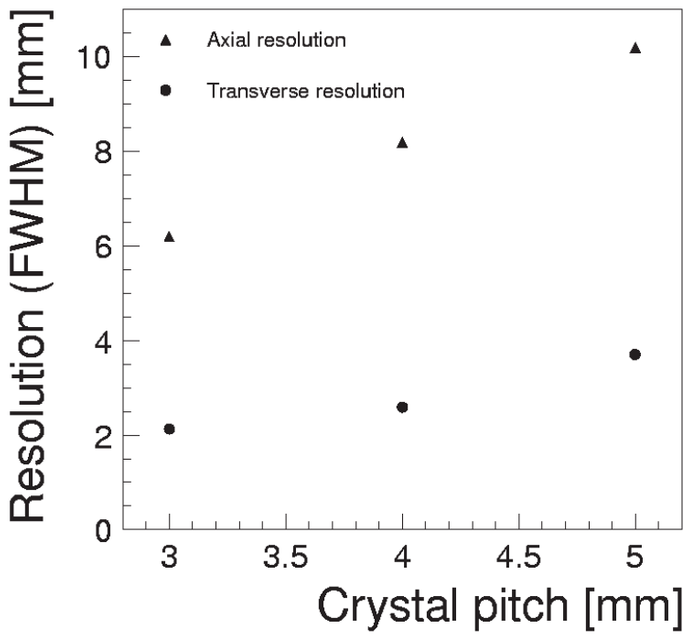

Fig. 14. Monte Carlo estimation of the transverse (dots) and axial (triangles) space resolution of PET systems based on 6×6 arrays of $3 \times 3 \times 25$ mm^3, $4 \times 4 \times 25$ mm^3 and $5 \times 5 \times 25$ mm^3 individually read-out LSO crystals. The space resolution is shown as a function of the crystal pitch.

4.3 Experimental study of the prototype of the PET detection system based on the LSO/SiPM detectors

The experimental study of the new detection system on the basis of LSO/SiPM photo-detectors for applications in medical imaging systems was performed on a prototype of PET detection system. The prototype consists of two LSO crystals coupled to a SiPM and positioned opposite to each other at 180°. The experimental setup is shown in Fig. 15a. The scintillator crystals used in this study are two $2.5 \times 2.5 \times 15$ mm^3 LSO crystals wrapped in two layers of 1.25 mm thick Teflon films. The crystals are fixed to two mechanical holders (plastic) and are positioned opposite to each other on an optic bench in a light tide environment. The distance between the LSO crystals is 1 cm in order to increase the acceptance angle for the efficient collection of the statistics. A SiPM is coupled to the surface of the LSO crystals without any optics coupling material. The SiPMs used in the test setup are 1 mm^2 Silicon Photomultiplier SPM, produced by SensL (Stewart, 2008).

The SiPM signals are read out on 50 Ω load resistors directly by 4 GHz Oscilloscope (Textronix TDS7404B) without any front end electronics. The signals is digitized with a sampling rate of 20 Gs/s, which corresponds to 100 ps time digitalising periods for two channels and 50 ps shift between the two signals.

A point-like positron source ^{22}Na is placed in the middle and aligned with the line of centers crystals connection. It is held by a thin plastic cylindrical support with 2 cm diameter and 2 mm thickness.

The digitized signal of the two SiPMs in coincidence correspondent to two 511 keV gamma quanta is shown in Fig. 16. The signal has typical amplitude of about 100 mV. The rise

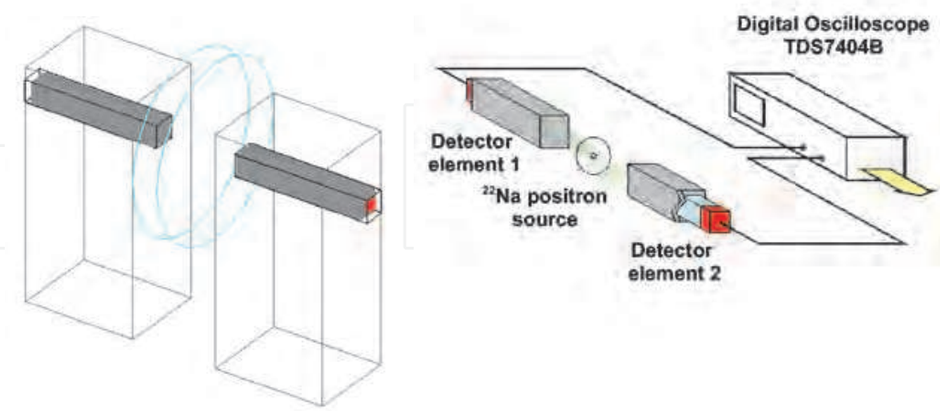

(a) (b)

Fig. 15. Mathematical model (a) and experimental setup (b) for the analysis of two LSO/SiPM (blue/red) system.

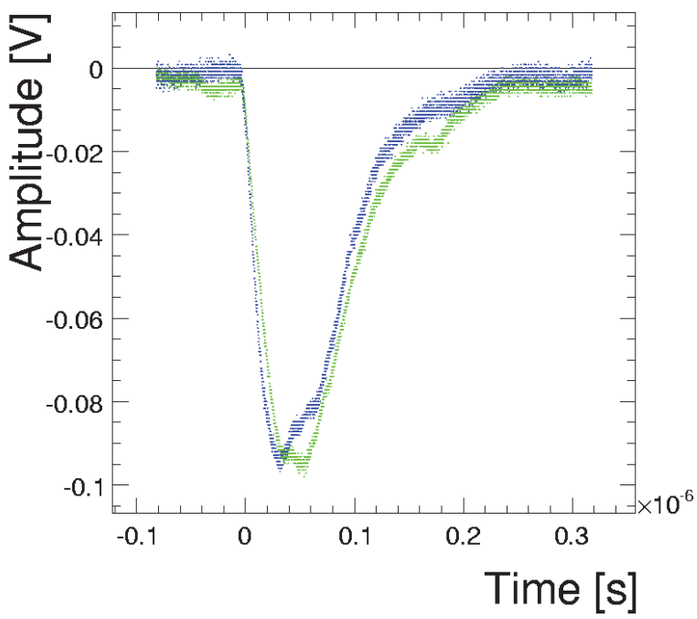

Fig. 16. Example of digitized signal of the two SiPMs (blue and green) when the annihilation photons from the ^{22}Na are detected in coincidence in the two opposite LSO crystals in the experimental setup.

time is 28 ns at the levels 10%-90%. The decaying component of the signal follows an exponential distribution with typical decay time of about 60 ns. The fully digitized signal gives a unique possibility to use powerful mathematical tools for the analysis of the main

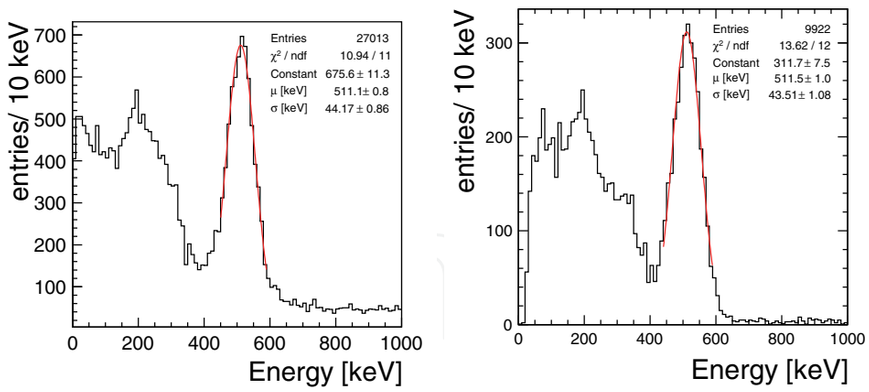

(a) (b)

Fig. 17. Monte Carlo (a) and experimental data estimation (b) of the energy resolution in the experimental setup.

characteristics of the detection system based on the LSO/SiPM and for the precise verification of the mathematical model.

4.3.1 Energy resolution of the LSO/SiPM detection system

The energy spectrum measured in the test setup is shown in Fig. 17b. The energy deposited in the LSO crystal (number of photons detected in the SPM) are calculated as the integral of the output signal. The integration is performed in an off-line analysis of the stored digital waveforms of the two SPM signals. The typical features of a γ-ray spectrum can be individuated: the photoelectric-peak at the energy of incident photons (511 keV), the Compton continuum extending from the photo-electric peak down to the instrumentation threshold and the back-scatter peak at around 200 keV, due to the Compton interaction of the incident photon in the material around the crystal.

The energy resolution of the LSO/SiPM detection system for PET is defined in the region of the photoelectric peak as $R \equiv \left(\frac{\sigma}{511\ \text{keV}}\right)$, where σ is the total variance and 511 keV is the mean value of the photo-electric peak.

The experimental energy resolution at the photo-electric peak is estimated with a gaussian fit as $R = (8.51 \pm 0.23)$ %.

The energy resolution of a LSO/SiPM system could be described by the total variance σ as the sum in quadrature of five independent contributions:

$$\sigma = \sigma_{LSO} \oplus \sigma_{stat} \oplus \sigma_{pdf} \oplus \sigma_{opt} \oplus \sigma_{el} \tag{3}$$

The intrinsic variance of the scintillation photons generated in the LSO is represented by σ_{LSO}. According to the experimental estimations reported in section 4.2, it corresponds to a resolution of $R_{LSO} = \frac{4.41\sqrt{LY \times 0.511}}{LY \times 0.511} = 3.76\%$.

The contribution σ_{pde} describes the broadening effect caused by the not uniform detection efficiency in the spectral range of the scintillation emission. It is estimated as $\sigma_{pde}\,[\text{keV}]\,/511\,[\text{keV}] = (3.77 \pm 0.54)\%$ for the combination of LSO/SiPM with the radio-luminescence spectrum and photon detection efficiency.

The impact of the reflection properties of the Teflon adds to the overall variance as an independent constant term σ_{opt}.

The optical transmission contribution of the experimental setup is estimated with the Monte Carlo as $\sigma_{opt}\,[\text{keV}]\,/511\,[\text{keV}] = (2.78 \pm 0.05)\,\%$. Dedicated experimental estimation of this contribution is also reported in the literature (Herbert, 2006).
The noise of the read-out electronics contributes to the total variance with a constant term σ_{el}. It is estimated from the experimental data as $\sigma_{el}\,[\text{keV}]\,/511\,[\text{keV}] = (1.68 \pm 0.11\%)_{el}$.
The binomial photo-statistics of the detection of the scintillation photons in the SiPM is included in the term σ_{stat}.
The detailed analysis of σ_{stat}, σ_{LSO} and σ_{pdf} is performed in analytical form with a statistical model, taking into account the photo-statistics of the generation and propagation of the optical photons in the crystal, the detection in the SiPM and the optical properties of the detection system.
The probability distribution $P(n)$, which describes the number of photons n detected in the SiPM if a γ-ray is detected in the LSO crystal, is expressed as:

$$\begin{aligned} P\left(n\right) = \int\int \frac{1}{\sqrt{2\pi\sigma_{sc}^2}} e^{-\frac{\left(N_{ph}-N_{LY}\cdot E_\gamma\right)^2}{\sigma_{sc}^2}} \times \\ \times \frac{1}{\sqrt{2\pi N_{ph}\alpha\cdot\epsilon(\lambda)(1-\alpha\cdot\epsilon(\lambda))}} e^{-\frac{\left(n-\alpha\cdot\epsilon(\lambda)N_{ph}\right)^2}{2N_{ph}\alpha\cdot\epsilon(\lambda)(1-\alpha\cdot\epsilon(\lambda))}} dN_{ph} P\left(\lambda\right) d\lambda \end{aligned} \tag{4}$$

where:

- N_{LY} is the light yield of LSO (27000 photons/MeV).
- E_γ is the energy of the detected $\gamma-$ray. In this study $E_\gamma = 511$ keV.
- $\sigma_{sc} = 4.41 \cdot \sqrt{N_{LY} \cdot E_\gamma}$ is the intrinsic resolution of the LSO crystal for energy E_γ.
- $P\left(\lambda\right)$ is the radio-luminescence spectrum of LSO (Fig. 5).
- $\epsilon\left(\lambda\right)$ is the photo-detection efficiency of the SiPM (Fig. 5).
- α is the geometrical photon collection efficiency, which takes into account the photon losses due to the not perfect reflectivity of the crystal/Teflon surfaces. It depends on the geometry of the crystal and of the size of the SiPM.

The mean value of the detected photons $\bar{n}$ is from Eq. 4:

$$\bar{n} = \int n \cdot P\left(n\right) dn = \int \alpha \cdot \epsilon\left(\lambda\right) \cdot LY \cdot E_\gamma P\left(\lambda\right) d\lambda = \alpha \cdot \bar{\epsilon} \cdot LY \cdot E_\gamma \tag{5}$$

The second moment of the number of detected photons $\langle n^2 \rangle$ is:

$$\begin{aligned} \langle n^2 \rangle &= \int n^2 \cdot P\left(n\right) dn = \\ &= \alpha \cdot \bar{\epsilon} \cdot LY \cdot E_\gamma - \alpha^2 \cdot \langle \epsilon^2 \rangle \cdot LY \cdot E_\gamma + \alpha^2 \langle \epsilon^2 \rangle \sigma_{sc}^2 + \alpha^2 \langle \epsilon^2 \rangle \cdot LY^2 \cdot E^2 \end{aligned} \tag{6}$$

where the quantities are defined:

$$\bar{\epsilon} = \int \epsilon(\lambda) P\left(\lambda\right) d\lambda \qquad \langle \epsilon^2 \rangle = \int \epsilon^2(\lambda) P\left(\lambda\right) d\lambda \qquad \sigma_\epsilon^2 = \langle \epsilon^2 \rangle - \bar{\epsilon}^2 \tag{7}$$

The quantities $\bar{\epsilon}$ and σ_ϵ represent the mean value and the total spread of the photon detection efficiency weighted over the radio luminescence spectrum of the LSO. The variance of the detected photons $\sigma^2 = \langle n^2 \rangle - \bar{n}^2$ is :

$$\alpha^2 \bar{\epsilon}^2 \sigma_{sc}^2 + LY \cdot E_\gamma \cdot \alpha \cdot \bar{\epsilon}\left(1 - \alpha \cdot \bar{\epsilon}\right) + \sigma_\epsilon^2 \left[\sigma_{sc}^2 + LY \cdot E_\gamma \cdot \left(LY \cdot E_\gamma - 1\right)\right] \tag{8}$$

The analytic formula for σ_{LSO}, σ_{stat} and σ_{pdf} is extracted from Eq. 8:

$$\begin{aligned} \sigma^2_{LSO} &= \alpha \cdot \bar{\epsilon}^2 \sigma^2_{sc} \\ \sigma^2_{stat} &= LY \cdot E_\gamma \cdot \alpha \cdot \bar{\epsilon}\,(1 - \alpha \cdot \bar{\epsilon}) \\ \sigma^2_{pde} &= \sigma^2_{\epsilon}\left[\sigma^2_{sc} + LY \cdot E_\gamma \cdot (LY \cdot E_\gamma - 1)\right] \end{aligned} \tag{9}$$

The performance of the LSO/SiPM is estimated with the mathematical model of the test setup. The best achievable energy resolution of a $2.5 \times 2.5 \times 15$ mm^3 LSO crystal is calculated in the case the crystal is read-out over the full area at one side by a perfect detector with photon detection efficiency equal to 1 over the whole LSO emission spectral range. The response of the crystal is simulated to a monochromatic 511 keV photons directed to the centre of the crystal. The energy resolution at the photo-electric peak is estimated as $R = (4.73 \pm 0.06)$ %, which corresponds to a total number of about 8100 photons. The result can be interpreted using the statistical model in Eq. 3, with the values $\bar{\epsilon} = 1$, $\sigma_\epsilon = 0$, $\alpha = 8100/(27000 \cdot 0.511) = 0.587$ and $\sigma_{el} = 0$:

$$(4.73 \pm 0.06)\,\% = (3.76\%)_{LSO} \oplus (0.71 \pm 0.01)_{stat} \oplus (2.78 \pm 0.05\%)_{opt} \tag{10}$$

The scintillator/SiPM detection system has the potential to reach the intrinsic energy resolution of the scintillator itself. This estimation is in fact in good agreement with reported experimental results, where an energy resolution of (4.24 ± 0.01) % is obtained with a $3 \times 3 \times 15$ mm^3 LSO crystal read-out over the whole 3×3 mm^2 area by a SiPM (D'Ascenzo et al., 2007).

The energy spectrum calculated with the mathematical model corresponding to the conditions of the experimental measurements is shown in Fig. 17a. The typical features of a γ-ray spectrum can be individuated. An average number of 254 detected photons corresponding to the photoelectric peak is calculated in the mathematical model. The energy resolution is estimated with a gaussian fit around the photoelectric peak as (8.64 ± 0.18) %. The result of the mathematical model estimation is interpreted according to the analytic model in Eq. 3, with $\alpha\bar{\epsilon} = 254/(27000 \cdot 0.511)$:

$$\begin{aligned} (8.64 \pm 0.18)\,\% \approx\ & (3.76\%)_{LSO} \oplus (6.21 \pm 0.06\%)_{stat} \oplus \\ & \oplus (3.77 \pm 0.54\%)_{qpd} \oplus (2.78 \pm 0.05\%)_{opt} \end{aligned} \tag{11}$$

where σ_{opt} and σ_{LSO} are determined as described above, σ_{stat} is determined from direct calculation using Eq.9 and σ_{qpd} is determined from a subtraction in quadrature.

The measured energy resolution can be decomposed similarly in the independent components according to Eq. 3:

$$\begin{aligned} (8.51 \pm 0.23)\,\% \approx\ & (3.76\%)_{LSO} \oplus (5.79 \pm 0.74\%)_{stat} \oplus \\ & \oplus (3.77 \pm 0.54\%)_{qpd} \oplus (2.78 \pm 0.05\%)_{opt} \oplus \\ & \oplus (1.68 \pm 0.11\%)_{el} \end{aligned} \tag{12}$$

where σ_{el}, σ_{opt}, σ_{LSO} and σ_{qpd} are determined in Eq. 11 and σ_{stat} is determined subtracting in quadrature all the determined components from the overall measured resolution.

The experimental data are well described by the mathematical model and the results in Eq. 11 and 12 are in good agreement. This proves the accuracy of the mathematical model of the PET detection system on the basis of LSO/SiPM individual read-out.

The SiPMs used in the experimental set-up have a 1×1 mm^2 active area which is smaller than the crystal surface. Although their average photon detection efficiency in the LSO emission spectral region is around 20% (Fig. 5), the small active area limits the overall photon collection efficiency of the LSO/SiPM system.

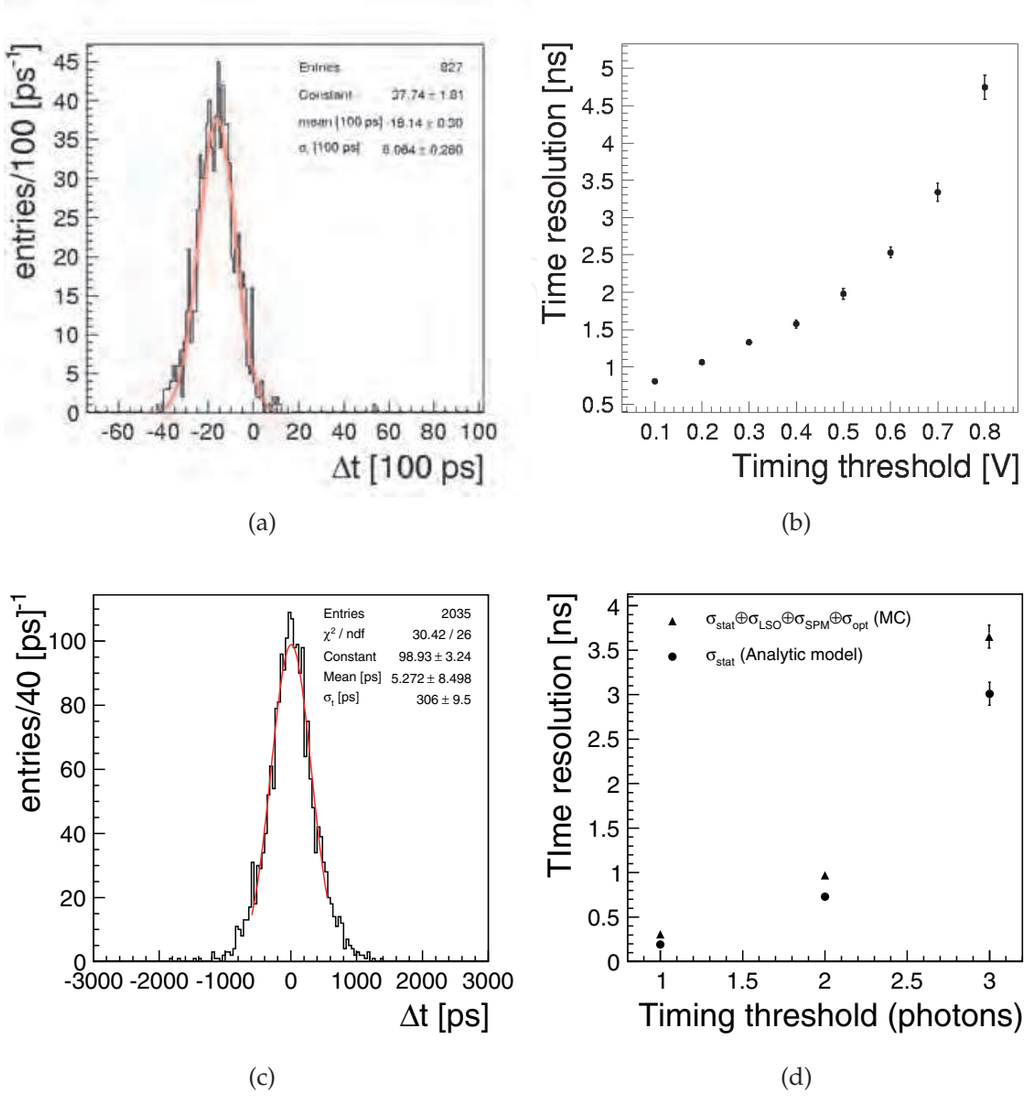

Fig. 18. Measured (a-b) and simulated (c-d) time difference distribution of two LSO/SPM detecting elements in coincidence of 511 keV signal from the β^+ emitter ^{22}Na. In (a,c) the timing threshold is set at $N_{ph} = 1$ photon. In (b,d) the time resolution is shown as a function of the timing threshold. The dots are the Monte Carlo estimation of the full energy resolution, the triangles are the analytical model described in Eq. 18.

4.3.2 Time resolution of the LSO/SiPM detection system

The measured time difference spectrum of the LSO/SiPM detection system in response to a Na^{22} source is shown in Fig. 18a. The events are selected in coincidence and if the integral of the corresponding signals is within a window of $\pm 3\sigma$ around the photo-electric peak. The threshold is selected to $N_{th} = -0.1$ V below the DC level of the signal. The time at which the signal crosses the threshold N_{th} is estimated with a linear fit around the negative edge of the detected signal. The mathematical simulation of the time response corresponding to the conditions of the experimental measurements is shown in Fig. 18c.

The time resolution $\sigma_t = 806 \pm 26$ ps is achieved from a gaussian fit to the coincidence time

spectrum.
The analysis of coincidence time resolution σ_t could be expressed as the sum in quadrature of five independent contributions:

$$\sigma_t^2 = \sqrt{2}\sigma_{LSO}^2 \oplus \sqrt{2}\sigma_{SPM}^2 \oplus \sigma_{stat}^2 \oplus \sigma_{opt}^2 \oplus \sigma_{el}^2 \tag{13}$$

where σ_{LSO} and σ_{SPM} are the time resolution respectively of LSO and SiPM.
The intrinsic time resolution of the SiPM σ_{SPM} is estimated from the rise time of the single photoelectron signal and is experimentally determined as $\sigma_{SPM} \sim 27$ ps (Saveliev, 2010).
The intrinsic timing response of the LSO crystal σ_{LSO} to 511 keV photons depends on two physics processes. The first is the time required for a 511 keV photon to undergo a photo-electric absorption. The second is the transit time of the photo-electron in the LSO crystal which determines the rise time of the scintillation photons emission. This means that if a 511 photon interacts through photoelectric effect in the LSO crystal within a mean free path λ, this process happens on average within $\sigma_{LSO} = \lambda/c \sim 29$ ps, where c is the speed of light.
The intrinsic overall coincidence time resolution of a LSO/SiPM detection system can be estimated as $\sqrt{2}\sigma_{LSO} \oplus \sqrt{2}\sigma_{SPM} = \sqrt{2} \cdot \sqrt{29^2 + 29^2} \sim 60$ ps.
The photo-statistics of the detection of scintillation optical photons, the optical properties of the Teflon/LSO surface and the read-out electronics affect significantly the overall coincidence time resolution of the LSO/SiPM detection system.
The contribution of the band-width and of the time-jitter of the read-out electronics introduces a constant finite resolution σ_{el}^2.
The reflection of the optical photons in the LSO/Teflon surface introduces a significant contribution to the coincidence time resolution at low photon fluxes. This effect is included in the overall coincidence time resolution with a constant term σ_{opt}. Its contribution to the coincidence time resolution of the LSO/SPM detection system is estimated with the Monte Carlo as $\sigma_{opt} \approx 250$ ps for the experimental setup.
The effect of the binomial photon detection efficiency to the detection of the timing threshold N_{th} photon is included in the term σ_{stat} and can be described analytically with a statistical model.
The contribution of the photo-statistics σ_{stat} is the variance of the probability distribution which describes the statistical process that after r intervals Δt, more than k photons are detected in the SiPM. The timing threshold is k detected photons. The distribution $P(t)$ of the detected scintillation photons is composed of two parts, according to the signal shape of the LSO/SPM system. It is approximately increasing linearly in the time range $(0, \tau_r)$ and is exponentially decreasing in the time range $(\tau_r, +\infty)$:

$$P(t) = \begin{cases} \frac{\bar{\epsilon}\alpha LY \cdot E_\gamma}{\tau \tau_r} t & 0 < t < \tau_r \\ \frac{\bar{\epsilon}\alpha LY \cdot E_\gamma}{\tau} e^{-\frac{t}{\tau}} & \tau_r < t < +\infty \end{cases} \tag{14}$$

where:

- LY is the light yield of the LSO crystal.
- E_γ is the detected energy in the crystal.
- τ_r is the rise time of the output signal of the detection system.
- τ is the average decay time of the LSO crystal.
- $\bar{\epsilon}$ and α are respectively the average efficiency of the SPM (Eq. 7) and the overall geometric photon detection efficiency.

The average value of the detected photons in the rth time interval is:

$$\mu\left(r\Delta t\right) = \int_{(r-1)\Delta t}^{r\Delta t} P(t)dt \tag{15}$$

The probability $P(n > k)$ of detecting more than k photons in the time interval Δt is described by the Poisson statistics:

$$P(n > k) = \sum_{n=k}^{+\infty} \frac{\mu^n\left(r\Delta t\right) e^{-\mu(r\Delta t)}}{n!} \tag{16}$$

The probability that more than k photons are detected after $r \times \Delta t$ ps is interpreted as the probability that more than k photons are detected at the r^{th} trial:

$$P\left(r\right) = \left(\sum_{n=0}^{k-1} \frac{\mu^n\left(r\Delta t\right) e^{-\mu(r\Delta t)}}{n!}\right)^{r-1} \times \left(\sum_{n=k}^{+\infty} \frac{\mu^n\left(r\Delta t\right) e^{-\mu(r\Delta t)}}{n!}\right) \tag{17}$$

which is expressed as:

$$P\left(r\right) = \left(1 - \sum_{n=k}^{+\infty} \frac{\mu^n\left(r\Delta t\right) e^{-\mu(r\Delta t)}}{n!}\right)^{r-1} \times \left(\sum_{n=k}^{+\infty} \frac{\mu^n\left(r\Delta t\right) e^{-\mu(r\Delta t)}}{n!}\right) \tag{18}$$

The variance σ of this distribution can be estimated numerically. It is a non decreasing function of the threshold value k. This statistical effect makes the measurement very sensitive to the chosen timing threshold, as observed also in other experimental studies (D'Ascenzo et al., 2007). The contribution of the photon statistics to the total coincidence time distribution is $\sigma_{stat} = \sqrt{2} \times \sigma$.

The best possible time resolution is $\sigma_t = (54.07 \pm 1.30)$ ps at a timing threshold of 1 detected photon in case of a $2.5 \times 2.5 \times 15$ mm^3 LSO crystal wth perfect read out at one side. The statistically independent contributions to the time resolution of the system are according to Eq. 13:

$$\begin{aligned}(54.07 \pm 1.30 \text{ ps}) \approx \sqrt{2}\,(29 \text{ ps})_{LSO} \oplus \sqrt{2}\,(29 \text{ ps})_{SPM} \oplus \\ \oplus\,(9.00 \pm 0.02 \text{ ps})_{stat}\end{aligned} \tag{19}$$

where σ_{LSO} and σ_{SPM} are taken from the above estimation and σ_{stat} is estimated numerically from the probability distribution in Eq. 18 with parameters $\bar{\epsilon} = 1$, $\sigma_\epsilon = 0$ and $\alpha = 8100/(27000 \cdot 0.511) = 0.587$. The contribution of the optical reflections on the boundary LSO/Teflon surfaces σ_{opt} is negligible at this high detected optical photon flux. The Monte Carlo results agree with the estimation of best possible coincidence time resolution of the LSO/SPM detection system shown above on the basis of physical principles.

The time difference spectrum of the LSO/SiPM detection system estimated with the mathematical model of the test setup is shown in Fig. 18a. The expected time resolution is calculated with a gaussian fit as 306 ± 9 ps at a timing threshold $N_{ph} = 1$ photon. The independent contributions to the time resolution are estimated according to Eq. 13 as:

$$\begin{aligned}(306 \pm 9 \text{ ps}) = \sqrt{2}\,(29 \text{ ps})_{LSO} \oplus \sqrt{2}\,(29 \text{ ps})_{SPM} \oplus \\ \oplus\,(191 \pm 5 \text{ ps})_{stat} \oplus (239 \pm 8 \text{ ps})_{opt}\end{aligned} \tag{20}$$

where σ_{LSO} and σ_{SPM} are taken from the above estimation, σ_{stat} is estimated numerically from the distribution 18 with parameters $\alpha\bar{\epsilon} = 254/(27000 \cdot 0.511)$ and σ_{opt} is calculated as a

difference in quadrature from the other terms.
The dependence of the coincidence time resolution on the threshold is estimated by simulation (Fig. 18b). The time resolution degradates from 306 ps up to about 3.6 ns when the threshold is increased from 1 up to 3 photons. The prediction of the analytical model for the statistical term σ_{stat} is also shown in Fig. 18b. The statistical term is a non decreasing function of the threshold. This explains the degradation of the estimated coincidence time resolution with the increase of the threshold. The difference between the modelling estimation and the statistical model depends on the additional terms σ_{LSO}, σ_{SPM} and σ_{opt} which are not included in the analytic model but are considered in the simulation.
The worsening of the coincidence time resolution with the increase of the coincidence timing threshold is also observed in the experimental data (Fig. 18d).
From a comparison between the dependence of the coincidence time on the timing threshold in data and the Monte Carlo, the timing threshold applied in the experimental data can be estimated as about 2 detected photons.
Improvements in the experimental set up are needed in order to achieve the expected time resolution of the LSO/SPM detection system.

5. Conclusions

The Silicon Photomultiplier technology is mature for the efficient read-out of scintillators, with consequent improvements in High Energy Physics and Nuclear Medicine applications.
The direct read-out of plastic scintillators by SiPM is feasible and can be an elegant solution for a simplification of the design of highly granular hadronic calorimeters in new high energy physics experiments.
The read-out of inorganic scintillators by SiPM is also a promising solution for the design of highly granular Positron Emission Tomographs of new generation, with transverse space resolution down to 2 mm and excellent time resolution of few hundreds ps.
The measured performances of the scintillator/SiPM detection system are hence promising for the possible applications to calorimetry and Positron Emission Tomography. In the latter case, a benefit is found both for morphological and functional in vivo studies in which space and time resolution play a significant role.

6. References

Alvares-Gaume L. et al. (2008) Review of Particle Physics, Particle Detectors. *Physics Letters*, Vol. 667, No. 1-5, 2008 , 281-370.
ATLAS Collaboration (1999) ATLAS detector and physics performance, CERN/LHCC99-14.
Behnke,T.; Damerell,C.; Jaros,J. & Miyamoto,A. (2007) ILC Reference Design Report. Vol4: Detectors, www.linearcollider.org/about/Publications/Reference-Design-Report
Blin,S. (2006) Dedicated very front-end electronics for an ILC prototype hadronic calorimeter with SiPM read-out, *LC-DET-2006-007*.
Boddaert N. & Zilbovicius V. (2006) Functional neuroimaging and childhood autism, *Pediatr.Radiol.*, 32, 1-7.
Buchsbaum et al. (1992) Brief Report: Attention performance in Autism and regional brain metabolic rate assessed by Positron Emission Tomography, *Journal of Autism and Developmental disorders*, 22, 115-125.
CALICE Collaboration (2010) Construction and Commissioning of the CALICE Analog Hadron Calorimeter Prototype, JINST 5 P05007.

The CDF II Collaboration (1996) CDF Technical Design Report, FERMILAB-Pub-96/390-E.

D'Ascenzo, N.; Eggemann A.; Garutti E. & Tadday, A. (2007) Application of Micro Pixel Photon Counter to calorimetry and PET, *Il Nuovo Cimento C*, Vol. 30 N.5.

D'Ascenzo,N.; Eggemann, A. & Garutti,E. (2007) Study of Micro Pixel Photon Counters for a high granularity scintillator-based hadron calorimeter, *DESY 07-196, arXiv:0711.1287*.

D'Ascenzo,N. (2009) Study of the neutralino sector and analysis of the muon response of a highly granular hadron calorimeter at the International Linear Collider, *Phd Thesis*, DESY-THESIS-09-004.

Firestone,R.B. (1996) Table of isotopes, New York Wiley.

Freeman,J. (2009) Silicon photomultipliers for the CMS hadron calorimeter, *Nucl.Instr.Meth.A*, 617, 393-395.

Golovin,V. & Saveliev,V. (2004) Novel Type of Avalanche Photodetector with Geiger Mode Operation, *Nucl.Instr.Meth.A*, 518, 560-564.

Herbert,D.J.; Saveliev,V.; Belcari,N.; D'Ascenzo,N.; Del Guerra,A. & Golovin,A. (2006) First results of scintillator read-out with Silicon Photomultiplier detectors, *IEEE Trans. Nucl.Sci.* NS53(1), 389-394.

ILD Concept Group (2009) The International Large Detector: Letter of Intent, *FERMILAB-LOI-2010-03*, *FERMILAB-PUB-09-682-E*, *DESY-2009-87*, *KEK-REPORT-2009-6*.

Karp,J.; Suleman,S.; Daube-Witherspoon,M.; Freifelder,R.; Cardi,C.A.; Adam,L.; Bilger,M. & G. Muehllehner, Performance of a Brain PET Camera based on Anger-logic gadolinium oxyorthosilicate detectors *Journ.Nucl.Med.*, 44, 1340-1349.

Mao,R.; Zhang,L. & Ramsden,D. (2002) Emission spectra of LSO and LYSO crystals excited by UV light, X-ray and γ-ray, *IEEE Trans. Nucl. Sc.*, 55, 1759-1766.

Melcher,C.L. & Schweitzer,J.S. (1992) Cerium-doped Oxyorthosilicate: A Fast, Efficient New Scintillator, *IEEE Trans. Nucl. Sc.*, 39, 1759-1766.

National Electrical Manufacturers Association (2001) Performance Measurements of Positron Emission Tomographs, NEMA Standard Publications NU-2-2001.

Yokoyama,M. (2009) Application of Hamamatsu MPPCs to T2K neutrino detectors, *Nucl.Instr.Meth.A*, 610, 128.

Saveliev V., Golovin V. (2000), Silicon Avalanche Photodiodes on the basis of Metal-Resistor-Semiconductor (MRS) Structures, *Nucl.Instr.Meth.A*, 442, 223-229.

Saveliev V. (2010), Silicon Photomultiplier - New Era of Photon Detection, Advances in Optical and Photonic Devices, Ki Young Kim (Ed.), ISBN: 978-953-7619-76-3, *InTech*.

SensL (2010), http://www.sensl.com.

Stewart,A.G.; Saveliev,V.; Bellis,S.J.; Herbert,D.J.; Hughes,P.J. & Jackson,J.C. (2008) Performance of 1 mm^2 Silicon Photomultiplier, *IEEE J. Quantum Electron*, 44(2), 157.

Strul,D.; Santin,G.; Breton,V. & Morel,C. (2003) *Nucl.Phys.B*,125,75-79.

Thompson,M. (2006) Particle Flow Calorimetry at the International Linear Collider, *Pramana journal of physics*, 69,6, 1101-1107.

Toshikaza Hakamata et al. (2006), Photomultipliers Tubes, Basics and Applications, Hammamatsu Photonics K.K., Electron Tube Division, Japan.

Tsang W.T. (Ed.) (1985) Semiconductors and Semimetals: Lightwave Communication Technology, Part D, Photodetectors, 1-309, Academic Press Inc., ISBN :978-0-12-752153-4.

Yamamura Kazuhisa et al. (2009) Production and Development status of MPPC, Proceedings of Science, PoS (PD09) 017.

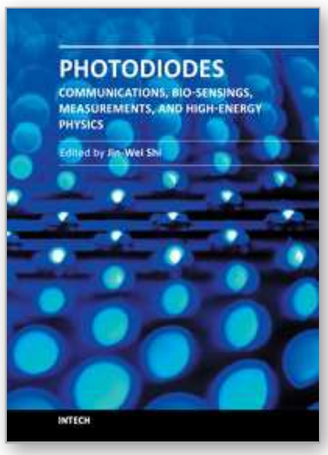

Photodiodes - Communications, Bio-Sensings, Measurements and High-Energy Physics

Edited by Associate Professor Jin-Wei Shi

ISBN 978-953-307-277-7
Hard cover, 284 pages
Publisher InTech
Published online 06, September, 2011
Published in print edition September, 2011

This book describes different kinds of photodiodes for applications in high-speed data communication, biomedical sensing, high-speed measurement, UV-light detection, and high energy physics. The photodiodes discussed are composed of several different semiconductor materials, such as InP, SiC, and Si, which cover an extremely wide optical wavelength regime ranging from infrared light to X-ray, making the suitable for diversified applications. Several interesting and unique topics were discussed including: the operation of high-speed photodiodes at low-temperature for super-conducting electronics, photodiodes for bio-medical imaging, single photon detection, photodiodes for the applications in nuclear physics, and for UV-light detection.

InTech Europe
University Campus STeP Ri
Slavka Krautzeka 83/A
51000 Rijeka, Croatia
Phone: +385 (51) 770 447
Fax: +385 (51) 686 166
www.intechopen.com

InTech China
Unit 405, Office Block, Hotel Equatorial Shanghai
No.65, Yan An Road (West), Shanghai, 200040, China
中国上海市延安西路65号上海国际贵都大饭店办公楼405单元
Phone: +86-21-62489820
Fax: +86-21-62489821

IntechOpen